

DOI: 10.1002/cmdc.200900282

Combined Pharmacophore Modeling, Docking, and 3D QSAR Studies of ABCB1 and ABCC1 Transporter Inhibitors

Ilza K. Pajeva,^[a, b] Christoph Globisch,^[a] and Michael Wiese^{*[a]}

Quinazolinones, indolo- and pyrrolopyrimidines with inhibitory effects toward ABCB1 (P-gp) and ABCC1 (MRP1) transporters were studied by pharmacophore modeling, docking, and 3D QSAR to describe the binding preferences of the proteins. The pharmacophore overlays between dual and/or highly selective inhibitors point to binding sites of different topology and physicochemical properties for MRP1 and P-gp. Docking of selective inhibitors into the P-gp binding cavity by the use of a structural model based on the recently resolved P-gp structure confirms the P-gp pharmacophore features identified, and re-

veals the interactions of some functional groups and atoms in the structures with particular protein residues. The 3D QSAR analysis of the dual-effect inhibitors allows satisfactory prediction of the selectivity index of the compounds and outlines electrostatics as most important for selectivity. The results from the combined modeling approach complement each other and could improve our understanding of the protein–ligand interactions involved, and could aid in the development of highly selective and potent inhibitors of P-gp and MRP1.

Introduction

The failure of chemotherapy in cancer treatment is mostly attributed to multidrug resistance (MDR). Supposed initially to be related to the transport P-glycoprotein (P-gp, ABCB1), MDR in tumor cells was later associated with other ABC transporters as well, such as the MDR-associated proteins (MRP, ABCC subfamily) and the breast cancer resistance protein (BCRP, ABCG2).^[1] All these proteins perform an ATP-dependent active outward transport of chemically unrelated compounds, including various antitumor drugs. Among the cancer MDR transporters, P-gp has been studied most extensively; in recent years, however, research interest has also been directed toward the ABCC family, among which MRP1 (ABCC1) has been investigated the most. Besides P-gp, MRP1 is known as a second major efflux pump in cancer MDR. Both proteins also act to protect normal tissues against xenobiotics. Like P-gp, MRP1 has a core structure that consists of two nucleotide binding domains (NBDs) and two multispansing transmembrane (TM) domains, each of which is composed of six segments followed by a NBD. In contrast to P-gp, MRP1 contains a third TM domain with five segments, preceded by a cytosol-exposed amino terminus and connected to the core ABC domain by a linker.^[2] Another difference between these transporters is their substrate specificity: MRP1 is an organic anion transporter, which, similarly to P-gp, can also extrude hydrophobic uncharged molecules, thus exerting a broader substrate acceptance.^[3]

In recent years, many compounds have been tested for their inhibitory activity against P-gp and MRP1. Correspondingly, a number of structure–activity relationship studies have been performed with the aim of getting a better understanding of the interactions between the inhibitors and the MDR transporters and to direct the synthesis of more potent and selective inhibitors of the efflux pumps (see reviews [4–6] and references

therein). Simultaneously, a number of dual inhibitors have been developed that show various affinities and selectivities against the proteins.^[7–9] Such data can be used specifically for analyzing the similarities and differences between drugs that interact with the transporters, thus helping to elucidate the binding preferences of the proteins. Additional opportunities for understanding the protein–inhibitor interactions are available from the recently resolved X-ray crystal structure of mouse P-gp, which has 87% sequence identity to human P-gp.^[10] The reported apo and drug-bound conformations correspond to the inward-facing structure of P-gp, which represents the initial stage of the transport cycle competent for binding drugs. Analysis of the large internal cavity, formed by the bundles of the TM domains, suggests a common mechanism of poly-specific drug recognition and thus could be used for direct modeling of drug binding.

The initial aim of this study was the identification of the pharmacophore differences between compounds with various effects toward MRP1 and P-gp. We rely on the data of Xenova Ltd., reported by Wang et al.,^[7–9] who synthesized and carried out in vitro studies of 111 compounds from the quinazolinone, indolo- and pyrrolopyrimidine classes; they outlined some highly selective as well as dual P-gp and MRP1 inhibitors. The

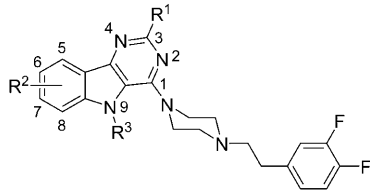
[a] Prof. Dr. I. K. Pajeva, Dr. C. Globisch, Prof. Dr. M. Wiese
Pharmaceutical Institute, University of Bonn
An der Immenburg 4, 53121 Bonn (Germany)
Fax: (+49) 228-737929
E-mail: mwiese@uni-bonn.de

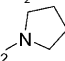
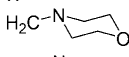
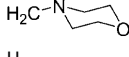
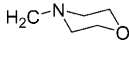
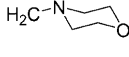
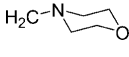
[b] Prof. Dr. I. K. Pajeva
Center of Biomedical Engineering, Bulgarian Academy of Science, Bl. 105,
Acad. George Bontchev Str., 1113 Sofia (Bulgaria)

Supporting information for this article is available on the WWW under <http://dx.doi.org/10.1002/cmdc.200900282>.

next aim of the work reported herein involved docking of the selective P-gp inhibitors into the protein binding pocket to validate the identified pharmacophore features and to reveal interactions between particular functional groups and atoms in the structures and protein residues. A structural model of human P-gp based on the reported 3D structure of mouse P-gp has been used. Finally, the data were analyzed in relation to the compounds' selectivity toward both proteins using molecular field analyses. Our results demonstrate that the pharmacophore preferences of the P-gp and MRP1 inhibitors have some similarity, but also show differences that relate to the number of the pharmacophore points involved in the interactions and their spatial location. Comparison of overlays of inhibitors with dual and/or highly selective effects in combination with docking into the P-gp binding cavity reveals that the MRP1 and P-gp binding sites certainly possess different geometric and physicochemical characteristics. The docking results confirm the role of the P-gp pharmacophore features identified and, for the first time, reveal the role of some functional groups and atoms in the structures of the third-generation MDR inhibitors with respect to their interactions with particular amino acids. The 3D QSAR analysis of the dual-effect inhibitors, carried out for the first time to estimate transporter selectivity, allows satisfactory prediction of compound selectivity and estimates electrostatics as a molecular field of primary importance for the selectivity. In general, the results of the applied modeling approaches complement each other in revealing the similarities and differences in the binding preferences and ligand interactions of the transporters.

Table 1. Structural and activity data of the indolopyrimidines studied.



	R ¹	R ²	R ³	pIC _{50(acc)} ^[a]		S _I ^[b]
				MRP1	P-gp	
I43	H	5-CH ₃	H	5.91	4.67	1.24
I44	H	6-NO ₂	H	6.88	5.04	1.84
I45	H	6-OCH ₃	H	6.09	5.08	1.01
I46	H	6-NHCOCH ₃	H	5.57	< 4.40	
I47	H	6-CO ₂ CH ₃	H	6.88	< 4.40	
I48	H	6-CONH ₂	H	5.46	< 4.40	
I49	H	6-SO ₂ - 	H	6.63	5.48	1.15
I50	H	5-Cl	H	6.44	4.76	1.67
I51	H	5-CN	H	6.56	4.94	1.62
I52	H	5-CONH ₂	H	6.74	4.55	2.19
I53	H	5-CONHPy-4	H	6.19	4.61	1.58
I54	H	5-NO ₂	H	6.74	4.74	1.99
I55	H	5-NH ₂	H	5.72	4.56	1.17
I56	H	7-OCH ₃	H	5.50	< 4.40	
I57	H	7-OCH ₃ , 8-NO ₂	H	5.46	< 4.40	
I58	H	5-NO ₂ , 6-OCH ₃	H	7.11	< 4.40	
I59		6-NO ₂	H	6.17	4.85	1.33
I60		6,8-di-NO ₂	H	6.93	5.09	1.84
I61	H	5-NO ₂	CH ₃	6.83	5.00	1.83
I62	H	5-NO ₂	Ph(CH ₂) ₂	6.65	5.16	1.50
I63	H	5-NO ₂	CH ₂ Py-3	6.21	5.16	1.05
I64	H	5-NO ₂	CH ₂ Py-4	7.10	5.21	1.89
I65	H	5-CONH ₂	CH ₃	7.21	< 4.40	
I66	H	5-CONH ₂	CH ₂ CO ₂ Et	6.91	5.04	1.88
I67	H	5-CONH ₂	CH ₂ Py-4	6.57	< 4.40	
I68	H	6-NO ₂	CH ₂ CO ₂ Et	6.86	4.98	1.88
I69		5-CONH ₂	CH ₃	6.64	< 4.40	
<i>N</i> heteroatom at position 6:						
I70	H	H	CH ₃	7.36	4.65	2.71
I71	H	H	CH ₂ Ph	6.26	5.08	1.19
I72	H	5-Cl	CH ₃	6.89		
I73	H	5-OCH ₃	CH ₃	6.76		
I74	H	5-OiPr	CH ₃	6.58		
I75	H	5-N(CH ₃) ₂	CH ₃	6.78		
I76	H	5-NHCH ₃	CH ₃	6.94		
I77	H	5-NHCH ₂ Py-2	CH ₃	6.98		
I78	H	morpholine	CH ₃	7.15		
I79	H	5-CH ₃	CH ₃	7.48		
I80	H	7-Cl	CH ₃	5.92		
I81	CH ₂ OCH ₃	5-Cl	CH ₃	6.61		
I82		5-Cl	CH ₃	7.05		
<i>N</i> heteroatom at position 5:						
I83	H	H	CH ₃	6.57		
<i>N</i> heteroatom at position 8:						
I84	H	5-CN	CH ₃	6.45		
I85	H	5-CN, 7-CH ₃	CH ₃	5.90		
I86	H	5-CONH ₂ , 7-CH ₃	CH ₃	6.65		
I87	H	5-CONH ₂	CH ₃	6.96		
I88	H	5-CONH ₂ , 6-NO ₂ , 7-CH ₃	CH ₃	7.06		
I89		5-CONH ₂	CH ₃	7.01		

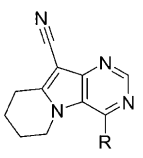
[a] Activity data for MRP1 and P-gp expressed as $-\log_{10}IC_{50}$ values obtained in daunorubicin accumulation assays.^[7-9] [b] Selectivity index: calculated as $[pIC_{50(acc)MRP1}] - [pIC_{50(acc)P-gp}]$.

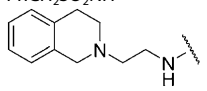
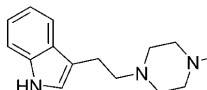
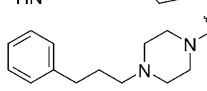
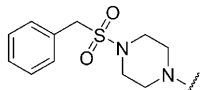
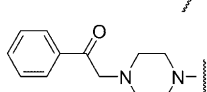
Results and Discussion

Preliminary analysis of the data

Tables 1–4 present the structures and activity data of the compounds studied as taken from the original reports.^[7–9] For clarity the same compound numbering is kept, and in order to distinguish between the same original compound numbers used for the different classes, a single letter has been introduced as a prefix that corresponds with the chemical class: **I**=indolopyrimidines (Table 1), **P**=pyrrolopyrimidines (Tables 2 and 3),

Table 2. Structural and activity data of pyrrolopyrimidines studied.



R	pIC _{50(acc)} ^[a]		S _I ^[b]
	MRP1	P-gp	
P25 PhCH ₂ CH ₂ NH	5.20	4.80	0.40
P26 PhCH ₂ CH ₂ NCH ₃	5.05	4.48	0.56
P27 PhCH ₂ SO ₂ NH	4.68	5.27	−0.59
P28 	6.20	< 4.30	
P29 	6.22	5.24	0.99
P31 	5.13	4.89	0.25
P32 	5.18	4.85	0.32
P33 	5.73	4.64	1.09

[a] Activity data for MRP1 and P-gp expressed as $-\log IC_{50}$ values obtained in daunorubicin accumulation assays.^[7–9] [b] Selectivity index: calculated as $[pIC_{50(acc)MRP1}] - [pIC_{50(acc)P-gp}]$.

and **Q**=quinazolinones (Table 4). The compounds have rather flexible structures and include various substituents at different positions of the parent scaffold. The activity data are expressed as pIC_{50(acc)} (i.e., $-\log IC_{50}$) values obtained in daunorubicin accumulation assays using similar protocols in the MRP1-expressing cell line COR.L23/R and the P-gp-expressing cell line EMT6/AR1.0. The selectivity is expressed as the difference between the pIC_{50(acc)} values for MRP1 and P-gp: $[pIC_{50(acc)MRP1}] - [pIC_{50(acc)P-gp}]$.

Figure 1 shows a plot of the pIC_{50(acc)} values for the compounds that were measured in both P-gp and MRP1 inhibition assays. In total, 74 compounds are shown (37 inhibitors are not given in the plot because of missing or undefined inhibitory data; Tables 1–4), generally revealing a lack of correlation

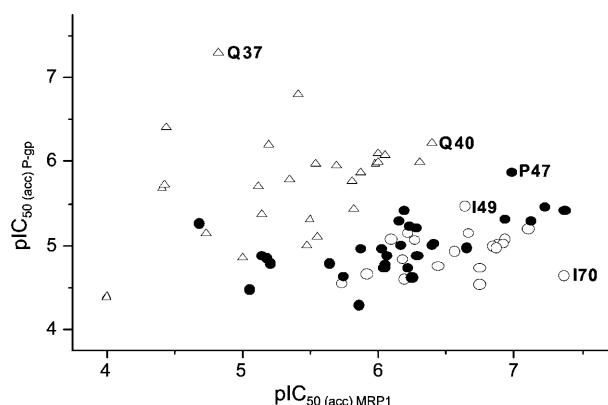


Figure 1. Plot of inhibitory activity of 73 compounds toward P-gp versus MRP1.^[7–9] **I**=indolopyrimidines (○), **P**=pyrrolopyrimidines (●), **Q**=quinazolinones (△). The most active selective (**Q37** and **I70**) and the dual inhibitors (**Q40**, **P47**, and **I49**) used in the study are labeled (see also Tables 1, 3, and 4).

between the P-gp and MRP1 pIC₅₀ values. Clearly outlined in the upper left part of the plot are three inhibitors from the **Q** class that inhibit P-gp and simultaneously have no or very poor MRP1 inhibitory potency: **Q37** (denoted on the plot), **Q32**, and **Q22**. In a reverse manner, some representatives of the **I** and **P** classes are potent MRP1 inhibitors with no or marginal effects toward P-gp, such as **I70** (denoted on the plot), **I65**, **I58**, **I47**, and **P55** (in the lower right part of the plot). For the most active MRP1 representative in the set **I78** (pIC₅₀=7.48) no P-gp activity was reported (Table 1). A number of inhibitors with dual activity, representatives of different classes, are spread around the midline, showing similar effects against P-gp and MRP1; among them **Q40** and **P47** are indicated on the plot as the most active dual-effect inhibitors representing different chemical classes. This data clustering has been taken into account in our research strategy described below.

Rationales of the research strategy

The inhibitors of the three chemical classes are flexible and can adopt various conformations within a narrow energy interval. The most potent inhibitors of the same protein (single most actives) will fit best into the corresponding protein binding site; the dual inhibitors with highest inhibitory effect (dual most actives) will fit into both binding sites, presumably by adopting different conformations suited to the particular binding site of either P-gp or MRP1.

A flexible overlay between the most active single and the best dual inhibitors could therefore map the most important common pharmacophoric features for binding to the particular protein binding site and help in outlining those functional groups and atoms that could explain the differences in their effects. Next, the flexible overlays between the most active single inhibitors and their comparison against the overlays with the dual inhibitors could help in the pharmacophoric mapping of the particular protein binding site. The best overlays will be selected based on formal (e.g., scoring values) and rational criteria (how well they explain the differences in the

effects observed). Docking experiments of selective P-gp inhibitors into the protein binding cavity will be further used to verify the P-gp pharmacophore features identified and to determine amino acids potentially involved in interactions with the ligands. The conformations generated from the pharmacophore alignments can finally be used for flexible alignment of all inhibitors to derive QSAR models for estimating a given compounds' selectivity toward P-gp and MRP1.

Pharmacophore alignments with dual inhibitors

The following pairs of the strongest single- and dual-effect inhibitors were studied: 1) **Q37** (the most active P-gp inhibitor with no effect on MRP1) in pairs with the most active dual inhibitors **Q40** and **P47**, and 2) **I70** (the strongest MRP1 inhibitor with a marginal P-gp inhibition effect reported in the set) with the same compounds. The structures of these compounds are shown in Figure 2.

Alignments on Q37

Figure 3 illustrates the pharmacophore alignments of **Q37** and the most active dual inhibitors **Q40** and **P47**. Generally, models of low specificity (max value 2.4, see Computational Methods below) were generated with **Q40** due to the high structural similarity between the compounds. Correspondingly, the models generated possess very good steric overlap, low total energy, and good pharmacophore concordance. Figure 3A shows the best two models obtained. In both models all functional groups and atoms are involved except the methoxy group at position 8 of **Q37** and the nitro group at position 6 of **Q40**, as well as one of the acceptor methoxy groups of the tetrahydroisoquinoline moieties. As observed from the overlay, the methoxy group of **Q37** and the nitro group of **Q40** point in rather different directions. Provided that the methoxy group

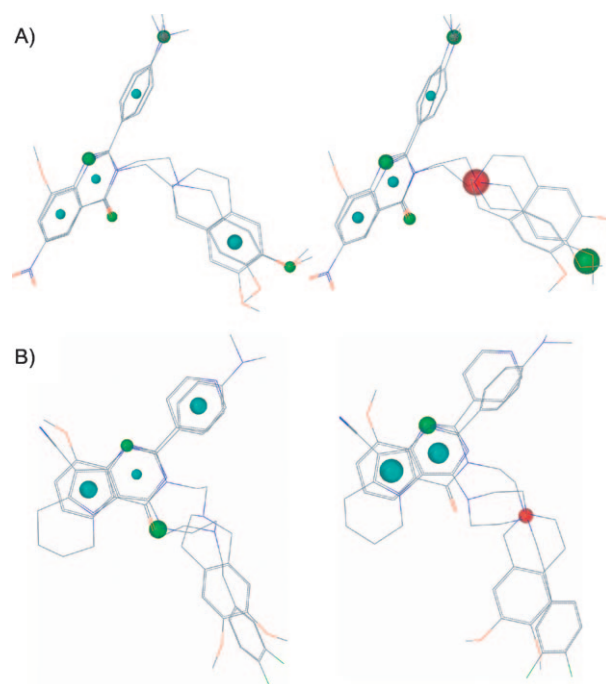


Figure 3. Pharmacophore alignments of the selective P-gp inhibitor **Q37** with the most active dual inhibitors: A) **Q40** and B) **P47**. Green = acceptor atoms, cyan = hydrophobic, red = positive nitrogen; the structures are colored according to the atom types, and hydrogen atoms are omitted.

forms a hydrogen bond (HB) within the P-gp binding site, the binding of **Q37** could be further stabilized by such an interaction. This suggestion could explain the increase in its inhibitory potency by about one log unit relative to **Q40** (P-gp pIC_{50} = 7.30 and 6.22 for **Q37** and **Q40**, respectively). The potential role of the methoxy group as a HB acceptor, however, has yet to be confirmed, as **Q37** is the only representative with such a group in the class.

Figure 3B shows the best models generated in the pharmacophore alignment of **Q37** and **P47** (P-gp pIC_{50} = 5.88). The model specificities are higher (from 4.2 to 4.3) than those obtained with **Q40**. The pyrrolopyrimidine and the quinazolinone ring systems as well as the side chain substituents do not achieve a good shape overlap especially when the tertiary nitrogen (colored in red) is involved. Besides the shape difference, the methoxy and cyano groups point in different directions, similarly to the overlay in Figure 3A.

Alignments on I70

Figure 4 illustrates the pharmacophore alignments of **I70** with the dual-effect inhibitors **Q40** and **P47**. The best model on **Q40** (Figure 4A) has four features and a specificity of 4.56. The nitro group at position 6 of the quinazolinone ring allows a HB acceptor interaction as does N6 in **I70**; furthermore, a second HB acceptor, one hydrophobic, and a protonated nitrogen function are identified. No hydrophobic feature in

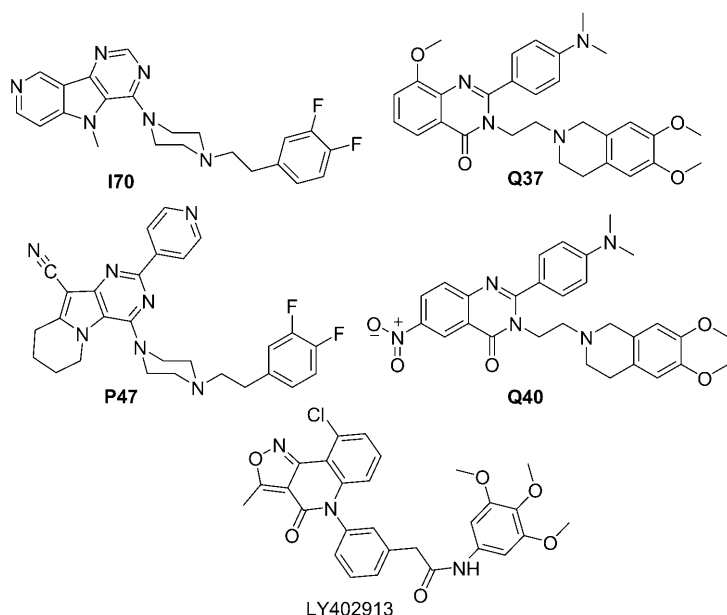


Figure 2. Structures of P-gp and MRP1 inhibitors used in the study.

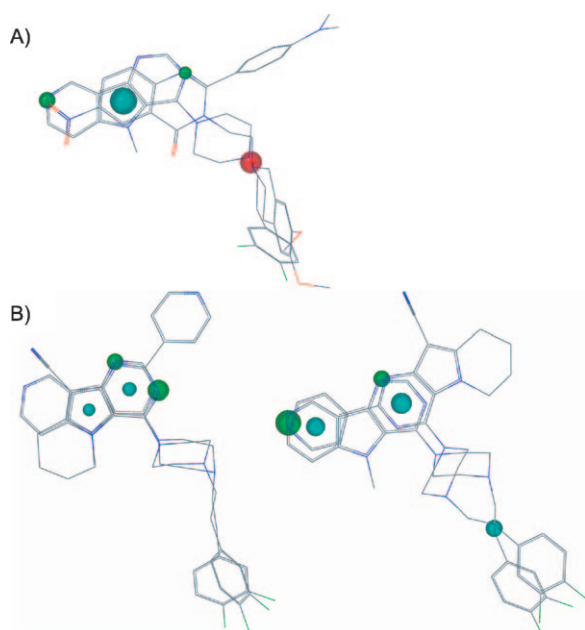


Figure 4. Pharmacophore alignments of the selective MRP1 inhibitor **170** with the most active dual inhibitors: A) **Q40** and B) **P47**. Green = acceptor atoms, cyan = hydrophobic, red = positive nitrogen; the structures are colored according to the atom types, and hydrogen atoms are omitted.

the aliphatic chain and involvement of the $-\text{N}(\text{CH}_3)_2$ -phenyl substituent were recorded. Considering that **Q40** is the most active MRP1 inhibitor in the quinazolinone class ($\text{pIC}_{50} = 6.40$), its pharmacophore overlay on **170** is in accordance with its effect.

The overlays of **170** and **P47** produced two mirror-like models with three and five features and specificities of 3.78 and 2.78, respectively, for the left and right overlays (Figure 4B). The left model consists of two hydrophobic and two HB acceptor points corresponding to the centroids and the N atoms in the planar indolopyrimidine ring system, respectively. The model at right identifies a HB acceptor point common to the N6 atom and the 4-pyridyl substituent at the R² position in the P class (Table 3); a common hydrophobic point in the side chain is also generated. The models involve different functional groups and no preference can be given to any of them. Thus, to decide on the important MRP1 pharmacophoric features, overlays of the most active MRP1 inhibitors were further performed.

MRP1 pharmacophore

Pharmacophore alignments of the most potent MRP1 inhibitors

Figure 5A presents the pharmacophore alignment generated with the most potent MRP1 inhibitors that show very low or no inhibition toward P-gp: **170**, **I65**, **I58**, **I47**, and **P55**. Compound **178** was also aligned, as it showed the highest MRP1 inhibitory effect in the whole set (Table 1). The compounds' ring systems share high similarity, correspondingly common hydrophobic ring centroids, and HB acceptors located on the pyrimi-

dine nitrogen atoms as well as on the piperazine nitrogen atoms were generated. Outlined is an additional HB acceptor point, located in the region of high structural variability, that corresponds to functional groups and atoms with acceptor functions such as N6 (compounds **178**, **170**), 6-OCH₃ (compound **I58**) and CONH₂ (compound **P55**) (Tables 1 and 3). There are two hydrophobic centers in the side chain: one is located on the CH₂ group in the chain between the piperazine and the difluorophenyl group, and a second is in the center of the latter. To outline the essential pharmacophores, this overlay was compared with the overlays of the most potent dual inhibitors (Figure 4). Besides the hydrophobic and acceptor points related to the common ring system and piperazine, an additional HB acceptor group at the ring system (labeled 'A' in Figure 5A) and a hydrophobic side chain end (assigned as 'H₂') appear as characteristic features of the most potent MRP1 inhibitors.

Figure 5B illustrates the MRP1 pharmacophore produced. Shown as spheres are the two endmost and two internal pharmacophore points related to the HB acceptor groups at positions 5 or 6 in the parent structure of indolopyrimidines or pyrrolopyrimidines (A), the hydrophobic center in the pyrimidine ring (H₁), the positive nitrogen (A/NP; here 'A' also suggests a HB acceptor function for an unprotonated nitrogen atom), and the hydrophobic center in the side chain phenyl ring (H₂). Notably, the distances between the adjacent points A, H₁, A/NP, and H₂ are very similar: between 5.1 and 5.5 Å.

Conformational analysis

To check the energetic feasibility of the pharmacophore conformations generated, they were compared with the local minimum conformers obtained from simulated annealing with subsequent energy optimization by molecular mechanics and quantum chemistry (see Computational Methods below). The simulated annealing of the most potent MRP1 inhibitors **178** and **170** resulted in 200 conformers, each within narrow intervals of the heat of formation: 0.2–7.00 kcal mol⁻¹ for **178**, and 9.96–16.6 kcal mol⁻¹ for **170**. The pharmacophore conformations extracted from the model were compared with the lowest-energy conformers, and the closest ones were identified according to the RMSD values. For **178**, the most similar conformer (RMSD = 1.35 Å of the heavy atoms) had an energy of 2.48 kcal mol⁻¹, and that for **170** (RMSD = 1.19 Å of the heavy atoms) had an energy of 12.56 kcal mol⁻¹, thus being 2–3 kcal above the energy of the global minimum conformers. The rigid fit of the pharmacophore groups and atoms in the pharmacophore conformations to these conformers resulted in even lower RMSD values (~0.5 Å), suggesting that the conformations produced by the pharmacophore alignment are reasonable and can correspond to the bioactive conformations of the most potent MRP1 inhibitors.

Alignment on LY402913

To further validate the importance of the identified pharmacophore features for MRP1 inhibition, we looked for a different

Table 3. Structural and activity data of pyrrolopyrimidines studied.

	R ¹	R ²	R ³	pIC _{50(acc)} ^[a]		SI ^[b]
				MRP1	P-gp	
P30	H	H	CN	6.16	5.02	1.14
P34	2-Cl	H	CN	6.02	4.98	1.05
P35	3-Cl	H	CN	6.04	4.75	1.29
P36	4-Cl	H	CN	6.40	5.04	1.36
P37	2-NO ₂	H	CN	5.85	< 4.30	
P38	3-NO ₂	H	CN	6.39	5.02	1.37
P39	4-NO ₂	H	CN	6.28	4.89	1.39
P40	3-OCH ₃	H	CN	5.64	4.79	0.85
P41	4-OCH ₃	H	CN	< 4.30		
P42	3-F, 4-F	H	CN	6.64	4.98	1.66
P43	H	I	CN	6.05	4.88	1.17
P44	H	Ph	CN	6.15	5.30	0.84
P45	H	4-CH ₃ CONHPh	CN	6.24	4.63	1.62
P46	3-F, 4-F	3-Pyr	CN	6.66		
P47	3-F, 4-F	4-Pyr	CN	6.98	5.88	1.10
P48	3-F, 4-F	2-CH ₃ Ph	CN	6.21	4.75	1.46
P49	H	H	COCH ₂ CH ₃	5.55	< 4.30	
P50	H	H	COPh	5.86	4.97	0.89
P51	H	H		6.04	4.78	1.26
P52	H	H		6.27	5.22	1.05
P53	H	H		6.19	5.43	0.76
P54	H	H		6.17	< 4.30	
P55	3-F, 4-F	H	CONH ₂	6.86	< 4.30	
P56	3-F, 4-F	H	CONH ₂ Et	6.92	5.32	1.6
P57	3-F, 4-F	H		7.37	5.43	1.93
P58	3-F, 4-F	H		7.22	5.47	1.75
P59	3-F, 4-F	H		7.12	5.31	1.81

[a] Activity data for MRP1 and P-gp expressed as $-\log IC_{50}$ values obtained in daunorubicin accumulation assays.^[7-9] [b] Selectivity index: calculated as $[pIC_{50(acc)MRP1}] - [pIC_{50(acc)P-gp}]$.

inhibitor that simultaneously shares some structural similarity to the studied inhibitors and which also has a high selectivity for MRP1. Compound LY402913 (Eli Lilly) is an isoxazole derivative that was identified as a potent MDR modulator with high selectivity for MRP1 over P-gp.^[11] Figure 6 shows the best models from the alignment of **178** and LY402913. The model shown in Figure 6 has the highest specificity (4.20) and consists of five features: three hydrophobic centers in the ring system (one of which corresponds to H₁), one in the hydropho-

bic end of the aliphatic chain (corresponding to H₂), and the acceptor point A, as present in the most active MRP1 inhibitors (Figure 5A). The distances between the identified points are 13.3 Å (A–H₂), 4.5 Å (A–H₁), and 9.7 Å (H₁–H₂), which are in very good agreement with those in the pharmacophore model (13.5, 5.5, and 9.7 Å, respectively). In neither of the alignments is the piperazine N2 of **178** involved, as there is no corresponding group in LY402913 as a positively protonated feature, according to the GALAHAD assignments. Notably, the piperazine N2 of **178** could act as an acceptor and could potentially be overlaid on the amide C=O group in LY402913 instead, resulting in a point closer to the A/NP point in the pharmacophore map. Thus, the pharmacophore alignment on LY402913 confirms the MRP1 pharmacophore identified above.

Interactions of quinazolinones with P-gp

Pharmacophore alignments of the most potent P-gp inhibitors

The three best selective P-gp inhibitors (**Q37**, **Q32**, and **Q22**) were overlaid pairwise and all together. **Q37** is the only compound with a pIC₅₀ value greater than 7.0; the other two compounds, **Q32** and **Q22**, have lower inhibitory potencies, with **Q22** being approximately one log unit less active than **Q37** (Table 4). The pharmacophore alignment of **Q37** and **Q32** produced pharmacophore models with all functional groups involved (except 8-methoxy in **Q37** and 5-chloro in **Q32**), but with different geometries (results not shown). Inclusion of **Q22** eliminated the generation of a model query for all three inhibitors with the tetrahydroisoquinoline moiety involved, most probably due to the long side chain with the CH₂-N-piperazine-N-2-pyrimidine substituent (Table 4). Putting these results together with the overlays of **Q37** on the best dual-effect inhibitors (Figure 3), it becomes clear once more that the high

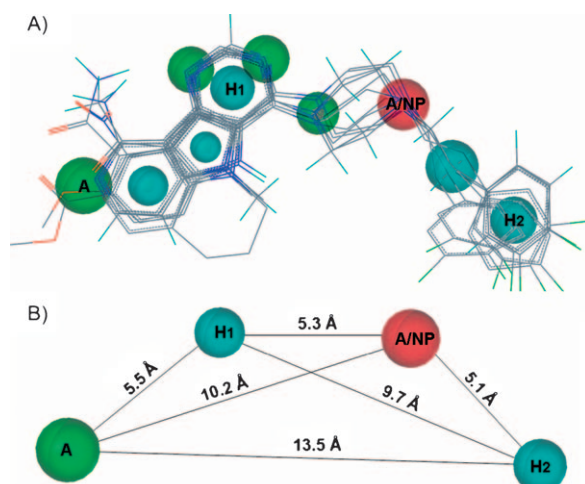


Figure 5. A) Pharmacophore alignments of compounds with high MRP1 and low P-gp inhibition activity (**I78**, **I70**, **I65**, **I58**, **I47**, and **P55**, located in the bottom right corner of Figure 1). B) Pharmacophore of the MRP1 inhibitors. Green = acceptor atoms, cyan = hydrophobic, red = acceptor/positive nitrogen; the structures are colored according to the atom types, and hydrogen atoms are omitted.

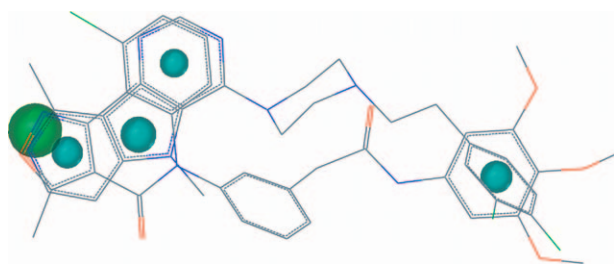


Figure 6. Pharmacophore alignments of **I78** and LY402913. Green = acceptor atoms, cyan = hydrophobic, red = acceptor/positive nitrogen, magenta = donor atoms; the structures are colored according to the atom types, and hydrogen atoms are omitted.

selectivity of this compound toward P-gp is mostly due to the presence of the 8-methoxy group in the quinazolinone ring. Additionally, a hydrophobic center in the tetrahydroisoquinoline substructure and a 7-methoxy group distinguishes the overlays of the **Q** compounds from that with **P47** (Figure 3B). To elucidate the potential role of the 8-methoxy and other functional groups and atoms for the inhibition effect of the selective P-gp inhibitors, a docking study was performed.

Docking of quinazolinones

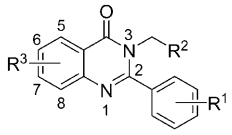
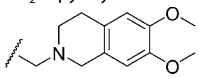
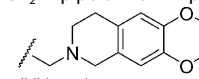
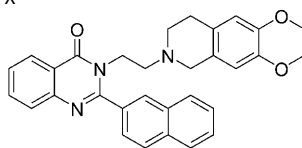
Four quinazolinones that differ by the substituent at position 8, **Q37** (-OCH₃), **Q36** (-CH₃), **Q35** (-Cl), and **Q18** (-H), were docked into the P-gp binding site (see Computational Methods below for human P-gp modeling). Figure 7 illustrates the compounds docked into the binding cavity of P-gp. In Figure 7A an overview of the whole cavity with the docked ligands is shown to give a presentation of the approximate location of the binding site; Figure 7B provides a closer view of the ligands' binding. The Gaussian contact surface clearly outlines the complex shape of the binding site (Figure 7B). It is predominantly hy-

drophobic and involves several amino acids. To outline the most consistent interactions between the ligands and the amino acids, a protein–ligand interaction fingerprint (PLIF) analysis was carried out. Two types of interaction were identified: amino acid side chain HB acceptor and surface contact interactions. Notably, a HB acceptor interaction was detected between the methoxy group of **Q37** and the hydroxy group of Tyr117 (TM2) at a distance of 3.2 Å (Figure 7B). Neither of the remaining compounds is able to perform such an interaction. The presence of a HB acceptor group in this position of the quinazolinone ring strengthens the interaction and explains the large difference in the inhibitory effects between **Q37** (pIC₅₀ = 7.30) and the other compounds (pIC₅₀ = 6.20, 5.98, and 5.97 for **Q36**, **Q35**, and **Q18**, respectively; Table 4). Next, for all four ligands, a HB acceptor interaction was observed between the 7-methoxy group at the tetrahydroisoquinoline moiety and the hydroxy group of Tyr307 (TM5). This result is in agreement with the pharmacophore point found at the same group in the overlay between **Q37** and **Q40** (Figure 3A). Surface contact interactions were identified for Phe336 (TM6), Tyr953 (TM11), and Phe957 (TM11) (Figure 7B). For the Tyr953 side chain ring, arene–arene interactions with the aromatic quinazolinone ring were detected using the ligand–protein interaction module in MOE. The influence of the substituent at quinazolinone on this interaction could be related to steric and electronic effects, because chloro and methyl groups are similar in size, but have different polar effects, whereas 8-chloro-substituted and unsubstituted compounds, although different in size, have very close inhibition activities.

The 4-N(CH₃)₂-phenyl group at R¹ of all inhibitors is located in a hydrophobic pocket surrounded by four hydrophobic phenylalanines: Phe72, Phe336, Phe732, and Phe978. Among them, Phe336 shows the most consistent surface contact interaction in the PLIF analysis. Clearly, bulky and hydrophobic substituents of a given size at R¹ could fit well to this pocket. Indeed, the R¹-unsubstituted **Q23** has pIC₅₀ = 5.10, while **Q25**, **Q30**, and **Q18**, with similar core structures and 4-isopropyl, 4-phenyl and 4-N(CH₃)₂ substituents, respectively, have almost equal pIC₅₀ values (6.00, 5.99, and 5.97) (Table 4).

No involvement of the amine nitrogen of 4-N(CH₃)₂-phenyl as a potential HB acceptor could be expected in this hydrophobic region, suggesting that the corresponding HB acceptor pharmacophore point might be an artifact (Figure 3A). Interestingly, neither the PLIF analysis nor the individual inspection of the ligand–protein interactions reveals the tertiary nitrogen in the tetrahydroisoquinoline substructure as a potential interaction point. The hydrophobic nature of the binding site does not suggest ionic interactions. Inspection of the binding cavity in the outward-facing conformation in the previously published homology model of P-gp^[12] reveals that all 12 amino acids in Figure 7B, except Phe732, remain exposed to the cavity, suggesting that the ligands may stay in contact with these amino acids in both inward- and outward-facing conformational states of the transporter. It could be speculated that in the outward-facing conformation the tertiary nitrogen becomes protonated, thus influencing specific residue contacts and decreasing the affinity of the ligand for the binding site.

Table 4. Structural and activity data of the quinazolinone compounds studied.

R ¹	R ²	R ³	pIC _{50(acc)} ^[a]		SI ^[b]	
			MRP1	P-gp		
						
Q4	4-N(CH ₃) ₂	CH ₂ -N-tetrahydroisoquinoline	H	5.50	5.30	0.19
Q14	4-N(CH ₃) ₂	<i>n</i> -pentyl	H	< 4.00	4.40	
Q15	4-N(CH ₃) ₂	cyclohexyl	H	5.00	4.85	0.15
Q16	4-N(CH ₃) ₂	Ph	H	< 4.00	4.39	
Q17	4-N(CH ₃) ₂	CH ₂ -4-pyridyl	H	5.48	5.00	0.48
Q18	4-N(CH ₃) ₂		H	5.98	5.97	0.01
Q19	4-N(CH ₃) ₂	CH ₂ -N-piperazine-N-Bn	H	4.41	5.68	-1.27
Q20	4-N(CH ₃) ₂	CH ₂ N(CH ₃)(CH ₂) ₂ -3,4-dimethoxyphenyl	H	4.43	5.72	-1.29
Q21	4-N(CH ₃) ₂	CH ₂ -N-piperazine-N-(3,4,5-trimethoxy)-Bz	H	5.14	5.38	-0.23
Q22	4-N(CH ₃) ₂	CH ₂ -N-piperazine-N-2-pyrimidine	H	4.44	6.41	-1.97
Q23	H	 = 'X' in subsequent entries	H	5.55	5.10	0.46
Q24	3-N(CH ₃) ₂	X	H	5.35	5.80	-0.45
Q25	4- <i>i</i> Pr	X	H	6.30	6.00	0.30
Q26	4-NEt ₂	X	H	< 5.00	5.89	
Q27	3- <i>n</i> Pr	X	H	6.00	6.10	-0.10
Q28	3,4-(OCH ₂ O)	X	H	5.82	5.43	0.39
Q29	2-OH	X	H	4.02		
Q30	4-Ph	X	H	6.00	5.99	0.01
Q32	4-N(CH ₃) ₂	X	5-Cl	5.42	6.80	-1.38
Q33	4-N(CH ₃) ₂	X	6-Cl	5.81	5.77	0.04
Q34	4-N(CH ₃) ₂	X	7-Cl	5.88	5.87	0.01
Q35	4-N(CH ₃) ₂	X	8-Cl	5.54	5.98	-0.44
Q36	4-N(CH ₃) ₂	X	8-CH ₃	5.20	6.20	-1.00
Q37	4-N(CH ₃) ₂	X	8-OCH ₃	4.82	7.30	-2.48
Q38	4-N(CH ₃) ₂	X	7-NO ₂	5.70	5.96	-0.26
Q39	4-N(CH ₃) ₂	X	7-NH ₂	4.73	5.14	-0.41
Q40	4-N(CH ₃) ₂	X	6-NO ₂	6.40	6.22	0.18
Q41	4-N(CH ₃) ₂	X	6-NH ₂	5.12	5.70	-0.58
Q31				6.05	6.07	-0.02

[a] Activity data for MRP1 and P-gp expressed as $-\log[\text{IC}_{50}]$ values obtained in daunorubicin accumulation assays.^[7-9] [b] Selectivity index: calculated as $[\text{pIC}_{50(\text{acc})\text{MRP1}}] - [\text{pIC}_{50(\text{acc})\text{P-gp}}]$.

However, the role of the tertiary nitrogen in the interactions of the ligands with the receptor remains to be elucidated.

The docking results confirm the importance of the HB acceptor group at position 8 of quinazolinone, the HB acceptor interaction of the methoxy group at position 7 of tetrahydroisoquinoline, the role of the hydrophobic quinazolinone ring, and the bulky hydrophobic substituent at R¹ for the P-gp-ligand interactions.

Table 5 lists the distances between the pharmacophoric points in the conformations of **Q37** extracted from the pharmacophore overlays with **Q32**, **Q40**, and from the docking. For the purposes of comparison with MRP1, the distances are shown using the same assignments for the pharmacophore

points that have their functional analogues in the MRP1 pharmacophore (Figure 5B). Additionally, distances related to the hydrophobic center in the R¹ phenyl ring (H₃) and the tetrahydroisoquinoline 7-methoxy group (A₁), not present in the MRP1 pharmacophore, are reported. As seen from the table, the distances in the conformations produced in the pharmacophore overlays on **Q32** and in the docked pose are nearly equal; however, in the conformations generated on **Q40** some distances vary significantly (shown in italics in Table 5) in correspondence with the lower inhibitory effect of this compound. Variations are also observed in the corresponding distances in the MRP1 pharmacophore (Figure 5B), suggesting different geometries of the binding sites of these inhibitors in P-gp and MRP1.

Conformational analysis

Similarly to the most selective MRP1 inhibitors, the **Q37** conformation, extracted from one of the best models in the overlays with **Q32**, was checked for consistency by an RMSD-based fit of the heavy atoms to the local minimum conformers generated after the simulated annealing and subsequent geometry optimization (see Computational Methods below). The 200 **Q37** conformers span an energy window of less than 5 kcal mol⁻¹

(from -70.4 to -65.7 kcal mol⁻¹ RM1 heat of formation). The conformation generated on **Q32** showed the highest similarity to the conformer with a heat of formation of -67.1 kcal mol⁻¹, and RMSD = 1.755 Å.

Pharmacophore alignments of the best selective inhibitors

We also performed a flexible pharmacophore alignment of the best single transporter inhibitors **Q37** and **I78**. As expected, no reasonable alignment could be produced. The models primarily involved one or two features and had low specificity (mostly 1.0). Occasionally models with three features were generated; however, these had extremely high energy values. Clearly, the

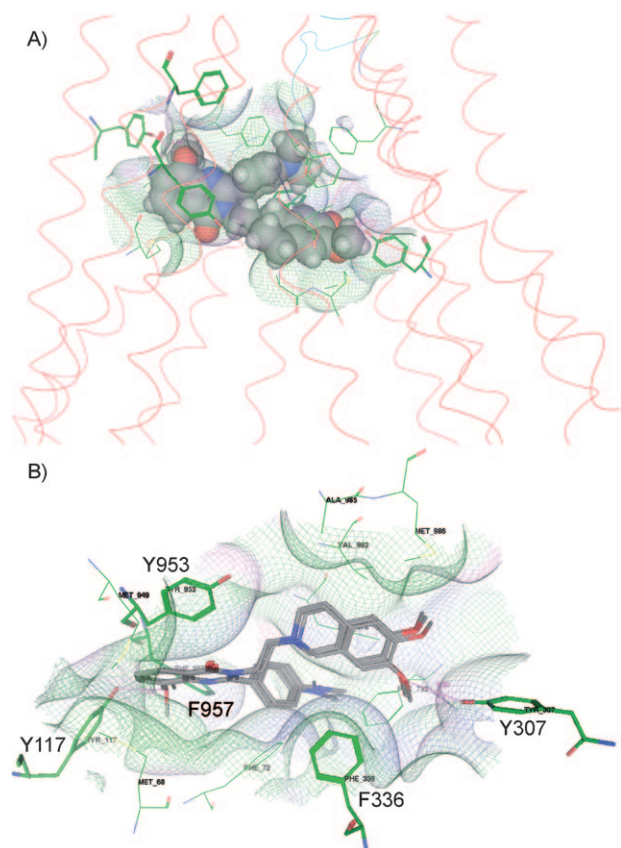


Figure 7. A) Front overview of the P-gp binding cavity with the inhibitors **Q37**, **Q36**, **Q35**, and **Q18** docked. B) Closer view (from the bottom) of the protein–ligand interactions and the surface of the binding site. The amino acids showing the most consistent interactions with the ligands in the PLIF analysis (Tyr 117, Tyr 307, Phe 336, Tyr 953, and Phe 957) are shown in stick representation, and the remaining amino acids as line structures. The Gaussian contact surface is represented by atoms with active lone pairs: green = hydrophobic, magenta = hydrogen bonding, blue = mild polar; the hydrogen bond lengths are colored in magenta, and the structures of the ligands are colored according to the atom types.

binding sites of P-gp and MRP1 differ in the pharmacophoric features of the most selective inhibitors.

3D QSAR study

Based on the results of the pharmacophore study, we further performed a 3D QSAR analysis to derive a model for estimating the compounds' selectivity for MRP1, using the difference $[pIC_{50(\text{acc})\text{MRP1}} - pIC_{50(\text{acc})\text{P-gp}}]$ as a dependent variable. A flexible alignment was used to overlay the compounds, with the assumption that they share some common shape (volume) complemented by hydrophobic and HB similarities when interacting with the particular binding site. Therefore, as a first step, a flexible alignment of three active dual-effect inhibitors was performed using representatives from each class (**Q40**, **P47**, and **I49**; Tables 1, 3, and 4). The rationale of this step is that all three compounds are able to interact with both MRP1 and P-gp binding sites, and thus could produce reasonable templates for aligning the rest of the compounds in the corresponding classes. The alignments were ranked according to the overall

Table 5. Distances between the pharmacophore points measured in the conformations of the most active P-gp inhibitor **Q37** extracted from the best models in the pharmacophore alignments on **Q32** (the second most active P-gp inhibitor), **Q40** (the best dually active inhibitor; Figure 3 A), and from docking (Figure 7 A).^[a]

Pairs of pharmacophore points	Distances [Å]		
	Pharmacophore alignment on: Q40	Q32	Docking pose
A–H ₁	3.7	3.7	3.7
A–H ₂	<i>9.5/10.1</i>	11.7/12.2	11.5
A–H ₃	6.1	6.1	6.1
A–NP	<i>6.4/6.6</i>	8.5/8.5	8.5
H ₁ –H ₂	<i>6.9/7.3</i>	8.3/8.7	8.4
H ₁ –H ₃	4.2	4.2	4.2
H ₁ –A/NP	<i>3.5/3.7</i>	5.0/5.0	5.0
H ₂ –H ₃	<i>8.0/7.6</i>	6.5/7.7	6.2
H ₂ –A/NP	3.8	3.8	3.7
H ₂ –A ₁	2.8	2.8	2.8 ^[b]

[a] The variable distances are shown in italics (for the meaning of the colors of the pharmacophore points, see Figures 3–6). [b] The distance is similar to the distance of A to the centroid of the aromatic ring next to H₁ in the quinazolinone substructure.

score value containing the similarity terms of the molecules both in combination with the strain energy, and by the strain energy separately. The selected alignment possessed the lowest strain energy and had the third-best overall score value. In the second step, the aligned dual active compounds were used as templates for the corresponding classes of inhibitors. The compounds of each class were aligned flexibly on the fixed (rigid) template structure. The final alignment of the compounds used in the selectivity analysis is illustrated in Figure 8.

The 3D QSAR analyses were performed using CoMFA and CoMSIA approaches applying leave-one-out (LOO) and leave-many-out (LMO) cross-validation. All single fields and all possible combinations were calculated. Three sets of compounds were analyzed depending on the reported activity values: 107 for MRP1, 77 for P-gp, and 73 for both transporters (selectivity set). For MRP1 the best model combined steric, electrostatic, and HB acceptor and HB donor fields; for P-gp the steric field produced the best model (data not shown). Table 6 summarizes the results of the 3D QSAR models generated with the selectivity set. The electrostatic field describes it in the best way with q^2 values of 0.732 in CoMSIA and 0.712 in CoMFA. Both models remain stable in the random group cross-validation and yield q^2 values greater than 0.7. None of the combinations with additional fields improves the predictive power of the resulting models. The next-best single-field models are the HB acceptor field in CoMSIA and the HB field in CoMFA followed by the steric fields. This result points to electrostatic properties

as contributing mostly to selectivity and indirectly suggests different 3D electrostatic profiles of the binding sites of MRP1 and P-gp.

Figure 9 shows the plot of the predicted versus observed selectivity values (LOO cross-validation) of the CoMSIA electrostatic field model. The linear regression is close to ideal, with an intercept of -0.01 ± 0.08 and a slope of 0.98 ± 0.07 . As evident from the plot and indicated by the correlation coefficient $r^2 = 0.82$, most compounds are predicted satisfactorily. However, two compounds deviate significantly: **Q37** and **I70**. **Q37** is the only compound that has a unique methoxy group with a strong influence on P-gp selectivity. **I70** is the most selective MRP1 inhibitor and is one of the two compounds in the I group with a nitrogen atom at position 6 (**I70** and **I71**, Table 1); the lower selectivity of **I71** could be related to the bulky benzyl substituent at R^3 .

In Figure 10 the SD*coefficient contour plots of the electrostatic-field-based CoMSIA model are shown with the structures of the dual inhibitors **Q40** and **P47** (Figure 10 A) and the most selective inhibitors **I70** and **Q37** (Figure 10 B). The dark gray contour defines a region where increased positive charge will result in increased selectivity toward MRP1 (or a more negative charge will result in increased P-gp selectivity). The light gray contour defines a region where increased electron density is favorable for selectivity toward MRP1 (or a decreased electron density is favorable for P-gp selectivity). The MRP1-selective compounds have a piperazine substituent in the central part of the molecule (light gray area); for the P-gp-selective inhibitors, the nitrogen atom in the tetrahydroisoquinoline is located in this region. The light gray contour on the left side of the structures corresponds mostly to the positive contribution of the fluorine substituents in the MRP1-selective compounds, and the light gray contour on the right is related to the presence of an acceptor group. The dark gray regions reflect the selectivity toward P-gp associated with low selectivity values (Tables 1–4). One of them is located in the vicinity of the carbonyl group, present in the structures of all quinazolones. The small dark gray region at the bottom part of

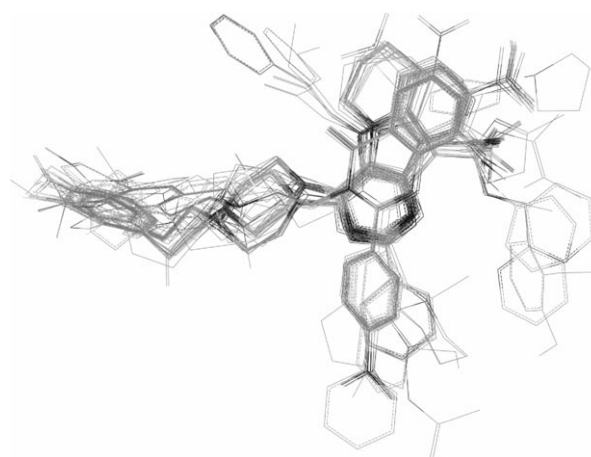


Figure 8. Alignment of the compounds involved in the selectivity analysis.

Table 6. Statistical characteristics of the 3D QSAR models for selectivity (MRP1 versus P-gp). ^[a]									
	q^2	LOO n_{opt}	PRESS	No validation r^2	s	LMO (5 groups) q^2_{mean}	SD	LMO (3 groups) q^2_{mean}	SD
CoMFA:									
b	0.703	2	0.571	0.775	0.497	0.704	0.013	0.694	0.022
s	0.637	5	0.645	0.912	0.318	0.634	0.023	0.629	0.026
e	0.712	2	0.562	0.770	0.502	0.708	0.017	0.702	0.024
hb	0.650	3	0.625	0.771	0.505	0.637	0.021	0.630	0.026
se	0.703	2	0.571	0.775	0.497	0.707	0.015	0.706	0.022
shb	0.658	3	0.617	0.807	0.464	0.646	0.012	0.645	0.020
ehb	0.691	3	0.586	0.806	0.465	0.677	0.015	0.675	0.027
bhb	0.682	3	0.595	0.824	0.442	0.690	0.011	0.676	0.026
CoMSIA:									
s	0.637	5	0.645	0.846	0.421	0.627	0.025	0.613	0.047
e	0.732	3	0.546	0.818	0.450	0.722	0.018	0.714	0.021
h	0.552	2	0.701	0.633	0.635	0.549	0.016	0.536	0.026
d	0.122	3	0.988	0.203	0.942	0.112	0.031	0.111	0.022
a	0.669	4	0.611	0.791	0.486	0.660	0.017	0.645	0.030
se	0.725	3	0.553	0.821	0.447	0.706	0.024	0.704	0.029
seh	0.714	3	0.565	0.816	0.453	0.709	0.021	0.681	0.031
sh	0.585	2	0.675	0.660	0.611	0.588	0.024	0.583	0.020
sd	0.592	6	0.689	0.793	0.491	0.593	0.018	0.592	0.037
sa	0.678	4	0.603	0.842	0.423	0.672	0.024	0.662	0.024
sda	0.658	4	0.621	0.775	0.504	0.646	0.016	0.644	0.035
shda	0.634	4	0.643	0.780	0.498	0.628	0.018	0.622	0.033
eh	0.714	4	0.568	0.839	0.427	0.704	0.021	0.683	0.044
ed	0.727	4	0.555	0.821	0.450	0.718	0.012	0.711	0.025
ea	0.714	3	0.564	0.813	0.457	0.708	0.015	0.712	0.015
eda	0.710	3	0.569	0.790	0.483	0.709	0.013	0.681	0.030
ehda	0.702	4	0.580	0.832	0.435	0.688	0.019	0.677	0.030
hda	0.626	4	0.650	0.761	0.519	0.610	0.020	0.608	0.030
ha	0.634	5	0.648	0.809	0.468	0.622	0.021	0.620	0.021
da	0.652	4	0.627	0.752	0.530	0.645	0.013	0.632	0.022
sehd	0.701	4	0.581	0.847	0.415	0.689	0.024	0.675	0.040
sehda	0.691	4	0.591	0.846	0.417	0.681	0.024	0.680	0.037
seda	0.705	3	0.574	0.793	0.480	0.694	0.017	0.684	0.022

[a] The best performing models are listed in bold. Fields: b = both, s = steric, e = electrostatic, hb = hydrogen bonds, h = hydrophobic, a = hydrogen bond acceptor, d = hydrogen bond donor; Statistical parameters: q^2 = cross-validated correlation coefficient, n_{opt} = optimal number of components, PRESS = predictive sum of squares, r^2 = correlation coefficient, s = standard error of estimate, q^2_{mean} = mean cross-validated correlation coefficient from the LMO runs, SD = standard deviation.

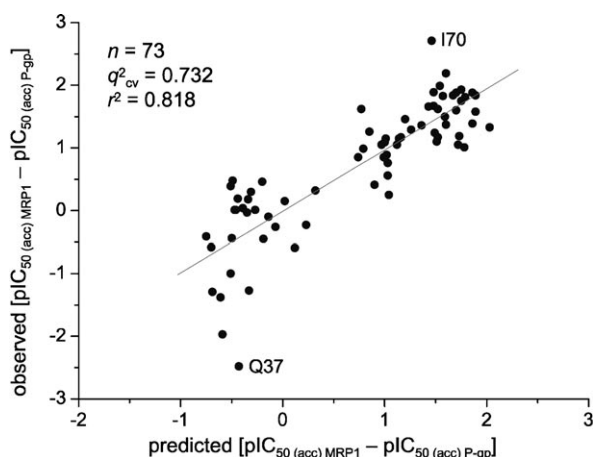


Figure 9. Predicted versus observed selectivity values obtained with the CoMSIA electrostatic model by LOO validation: n = number of dual inhibitors used, q^2_{cv} = LOO cross-validated correlation coefficient, r^2 = linear fit correlation coefficient, line intercept = -0.01 ± 0.08 , slope = 0.98 ± 0.07 .

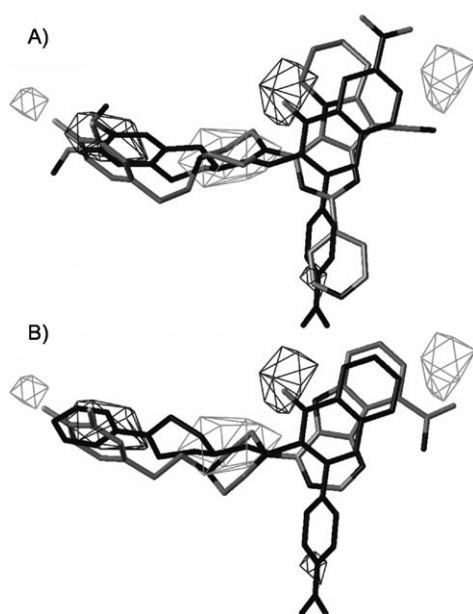


Figure 10. Contour plot (SD*coefficient; levels: 80% favored, 20% disfavored) of the CoMSIA model based on the electrostatic field (see Table 6) with A) the best inhibitors **Q40** and **P47** and B) two of the most selective MRP1 (**I52**) and P-gp (**Q22**) inhibitors. Dark gray = favored, light gray = disfavored; hydrogen atoms are omitted.

the figure corresponds to the amino group of the quinazolinones; however, as shown by the analysis of the docking results, the increase in P-gp selectivity is associated with the presence of a bulky alkyl-substituted amino group in this region. The dark gray region on the left is related to the presence of aromatic substituents in this part of the molecules and additionally reflects the contribution of the methoxy groups at the tetrahydroisoquinoline-substituted quinazolinones. Generally, the selectivity contour plots outline the influence of those regions in the structures where the pharmacophore points of importance for MRP1 and P-gp selectivity are located.

Comparison with other studies

Elucidation of the pharmacophore patterns of compounds that are able to interact with ABC transporters is consistently a focal point of research interest. The most studied transporter is P-gp, for which a number of pharmacophores have been proposed,^[13–16] but recently MRP1 and BCRP have also been studied.^[17,18]

In discussions of pharmacophores related to a particular transport protein it is important to keep in mind that the protein–inhibitor interaction is driven by an induced-fit mechanism that presumes conformational changes in both the protein and inhibitor upon binding. Thus, the definition of a pharmacophore for either of these transporters can be found only when a particular set of inhibitors is considered, especially when the inhibitors possess various and flexible structures, as is the case with those studied here. This is in agreement with the recently obtained 3D structures of P-gp–ligand complexes suggesting poly-specific drug recognition mechanisms and the possibility to accommodate more than one compound simultaneously,^[10] this certainly holds true for most of the ABC transporters.

For the first time the pharmacophore of P-gp-related inhibitors described herein has been related to particular amino acids in the binding cavity of the transporter through the use of docking and fingerprint analysis. Among the amino acids involved in the pocket, Val982 and Ala985 have also been interpreted to interact with methanethiosulfonate-rhodamine and dibromobimane in several cross-linking experiments.^[19,20] Phe72, Tyr307, Phe332, Phe732, Tyr953, Phe978, and Val982 were found to be in close proximity to the QZ59 compounds in the P-gp complex.^[10] Inspection of the identity between the residues involved in the binding site of the studied P-gp inhibitors (Figure 7B) in the human and mouse P-gp sequences showed a full correspondence.

Thus, the putative binding site of the quinazolinone inhibitors might partially overlap with the binding sites of rhodamines, dibromobimane, and the QZ59 compounds. Currently ongoing docking studies suggest that the binding site of quinazolinones may also overlap with the binding site of tariquidar and its analogues (unpublished data). Comparison of the pharmacophore points identified for quinazolinones to those of the tariquidar-related compounds reported previously^[16] do suggest such a possibility. In both series a similar pattern of acceptor and hydrophobic points in alternating order appear in the compound structures: both contain a terminal methoxy-substituted tetrahydroisoquinoline, and the methoxy-substituted quinazolinone in the **Q** compounds resembles the methoxy-substituted anthranilamide in the tariquidar analogues. Future studies, not only on P-gp inhibitors, but also on P-gp substrates, will reveal the consistency of the P-gp pharmacophore patterns identified so far.

Studies with MRP1 are more recent than those of P-gp. Therefore, MRP1 has been less well characterized both experimentally and by modeling. One of the first MRP1 pharmacophores was published by Chang et al. using five diverse and potent MRP1 inhibitors.^[17] Three ring aromatic and two HB

acceptor features were obtained by the Catalyst HIPHOP software. Generally, this model agrees well with the MRP1 model derived in this study by having some correspondence to A, H₁, A/NP, and H₂ pharmacophore points (compare figure 3 in reference [12] and Figure 5B herein). Unfortunately, no details are given on the distances and particular groups involved; however, the model validation over 500 clinically used drugs has resulted in eight hits and roughly half of them have already been documented to have an MRP1 inhibition effect.

The data reported by Wang et al.^[7–9] used in this study have been explored by other research groups as well, and mostly in relation to the MRP1 inhibition potency of the compounds. Lather and Madan^[21] applied a distance-based topological index as a molecular descriptor to a set of 82 pyrrolopyrimidines to build up a classification model with 88% accuracy of prediction. Tawari et al.^[18] published an MRP1 pharmacophore of these compounds, but the proposed map was restricted only to common functional groups and atoms in the structural skeleton, thus omitting some features essential for interactions.

Conclusions

In this study we set out to identify the similarities and differences in the pharmacophore patterns of inhibitors of both ABCC1 (MRP1) and ABCB1 (P-gp) transporters, making use of MRP1 and P-gp inhibition effects of the compounds, and by combining various modeling techniques. A summary of the results follows:

The MRP1 and P-gp pharmacophores are similar regarding the presence of:

- At least one HB acceptor group (A) of limited flexibility either as a substituent directly attached to, or as a heteroatom in, a planar hydrophobic ring system (H₁). The A group is crucial for the inhibitory activity of the compounds against both P-gp and MRP1. Its role for the MRP1 inhibition effect was not identified in the previous pharmacophore study on the same group of inhibitors.^[18]
- An additional hydrophobic center (H₂) in a flexible side chain attached to the planar hydrophobic ring system and located farthest from A.
- A tertiary protonatable nitrogen that could act as either HB acceptor or HB donor (denoted by A/NP). Relative to A, A/NP has higher flexibility and is located between H₁ and H₂. The role of A/NP as either HB acceptor acting in the hydrophobic environment of the binding site in the inward conformation (high-affinity state) or as an ionic center driving drug release in the outward conformation (low-affinity state) remains to be elucidated.

The differences relate to:

- The position and directionality of A: in both transporters this group may occupy different positions, suggesting different directionality of this HB acceptor interaction in the binding sites. Notably, the lower the flexibility of A, the

higher the effect of the MRP1 inhibitors: the most active MRP1 inhibitors have a heteroatom in the ring system (**I78**, **I70**) or an amide oxygen attached directly to the ring system (**P57**). In **Q37** the HB acceptor A is directly attached to the ring system, and the methyl group also restricts its flexibility.

- Involvement of an additional acceptor in the case of P-gp, corresponding to the 7-methoxy group at the tetrahydroisoquinoline substructure. Our previous studies have shown that the methoxy groups at the tetrahydroisoquinoline have a significant effect on the inhibitory potency of the P-gp inhibitors, analogues of tariquidar,^[22] but the particular role of these groups (electronic, steric, or HB acceptor functions) remained unclear. The docking results in this study reveal for the first time their role as HB acceptors.
- The distances between the pharmacophore features of similar functionality differ between P-gp and MRP1. In the case of MRP1 the features appear at a regular step of ~5 Å (Figure 5B); in the case of P-gp these distances vary significantly (Table 5).

For P-gp, the 3D structure for which is already available, direct relations could be done to particular amino acids involved in the interaction. For MRP1, two putative binding sites have been proposed: one with a relatively high affinity for glutathione, GSH (G-site) and a low affinity for the drugs, and one with a relatively high affinity for the drugs and low affinity for GSH (D-site).^[23] Presumably, the MRP1 pharmacophore, identified in this study, relates to the D-site of MRP1. This is the MRP1 binding site that corresponds more closely to the P-gp binding site, in agreement with the presentation for similar drug binding domains of MDR transporters.^[24] Thus, the differences observed in the binding preferences between the selective P-gp and MRP1 inhibitors could possibly be related to differences in the geometry and physicochemical characteristics of the drug binding sites of both transporters.

In general, the results of the combined pharmacophore, docking, and 3D QSAR modeling study correspond and complement each other in revealing important structural features and could be helpful for the development of highly selective and potent P-gp and MRP1 inhibitors.

Computational Methods

The programs MOE (v. 2008.10) and SYBYL (v. 8.1) were run on Linux workstations. The structures were built in MOE, as no X-ray crystallographic data were available. The following modeling techniques were applied: pharmacophore identification, conformational analysis, protein modeling and docking, flexible alignment, and 3D QSAR analysis.

Pharmacophore identification

This was performed with GALAHAD implemented in SYBYL. The program uses a genetic algorithm to generate pharmacophore hypotheses and alignments from sets of ligand molecules that bind at a common target site. The compounds were mostly run in groups of two to six compounds. The best 20 models were kept

and analyzed. The default settings were used for the advanced parameters. Repeated runs (minimum two) were performed using different seeds. The maximal number of generations and molecules to hit was defined as suggested from the data. The models generated were selected based on several criteria. The initial ranking was based on the so-called Pareto value: when equal to 0, Pareto indicates that no single model is superior to any other by criteria such as the total energy of the model, steric overlap, pharmacophoric concordance, and molecular query. In most cases models with a Pareto value of 0 were produced. In such cases the model properties were considered that were generated during the post-processing: the total number of features, the number of hits, and specificity (a logarithmic indicator of the expected discrimination of the query based on its number of features, their allotment across any partial match constraints, and the degree to which the features are separated in space). Pharmacophore models with high total energy (energy values that significantly exceeded those of the remaining models) were neglected. In rare cases models contained a ligand that failed to match the model query. The characteristic pharmacophoric features were indicated by a particular color of the associated spatial tolerances and macro spheres. The size of the spheres was proportional to the space where the features match. The distances between the points were calculated by the "Add Model Distance" option in the pharmacophore model analysis (PMA) menu of the spreadsheet.

Conformational analysis

The most selective compounds for the single transporters and the best dually active inhibitors were submitted to a conformational analysis by simulated annealing to explore their conformational space. The simulated annealing was performed in SYBYL with the MMFF94 force field and the following settings: 200 cycles, 1000 K initial temperature, 2000 fs equilibration, 0 K target temperature for 10000 fs annealing time, and exponential annealing function. The obtained 200 local minima were first optimized using the MMFF94x force field in MOE and then by MOPAC2007 with the semiempirical quantum chemistry method RM1 (full optimization, precise convergence, "MMOK" keyword).

Homology modeling of human P-gp

Preparation of the protein structure: In the template structure of mouse P-gp (PDB code: 3G61, chain A), the disrupted helix in TM12 (residues 982–1000) was replaced with the homologous part of TM6 (residues 339–357) by superposing the three terminal amino acids on the backbone atoms (Supporting Information, figure S1). The homology model of the template structure was minimized using the Amber99 force field in MOE with the ligands as environment. One hundred models were generated using the best intermediate option with medium minimization, including prevention of clashes only, to stay as close as possible to the initial structure. The final template model was selected according to the best score in the MOE scoring function.

Alignment: A multi-sequence alignment including the template (PDB code: 3G61, chain A), human MDR1 (Swissprot database code: P08183), and the closest relative to human P-gp (hamster MDR1, Swissprot database code: P21448) was performed by the "Align" tool in MOE with blosum62 substitution matrix, a gap penalty of 15, and a gap extension penalty of 2.

Model development: The final model was developed on the basis of the preprocessed template and included the co-crystallized

ligands as environment. One hundred models were generated using the best intermediate option and medium minimization with the Amber99 force field for each model to remove the bad contacts. The best model was selected according to the MOE scoring function and investigated by the protein report function in MOE. No outliers in the TM domains of the protein were found that are important for drug binding competency. The deviating amino acids (31 outliers), located mostly within the loop regions of the NBDs according to the report, were then minimized together with the adjacent amino acids, keeping the remaining protein fixed. After minimization, the outliers in the Ramachandran plot were decreased from 95 in the initial template structure to 31 in the initial model and to 20 after minimization. Supporting Information figures S2 and S3 show the Ramachandran plots and the location of the outliers within the X-ray crystal structure and the final protein model, respectively. The protonation state of the model was assigned by the protonate 3D module in MOE, which considers the solvent accessibility and regional neighboring of the amino acids.

Docking: The ligands were built in MOE, minimized with the MMFF94 force field, and subsequently exported as mol2 files for docking with the GOLD Suite (GOLD v. 4.0.1). The binding pocket was defined on the basis of the co-crystallized ligands in the X-ray structure, extended by 14 Å, and the outward-facing amino acids deselected; 20 solutions per molecule were calculated using the default setting for the genetic algorithm and the Gold score function.

PLIF analysis: Protein–ligand interaction fingerprints (PLIF) in MOE is a fingerprint scheme for estimation of the protein–ligand interactions. The amino acids of the protein are classified into categories according to the possible interactions split into types (side chain hydrogen bonds (donor or acceptor), backbone hydrogen bonds (donor or acceptor), ionic interactions, and surface interactions) and levels (low and high). The category could be assigned the following bit patterns: 00 (no interactions found, or none pass the thresholds); 10 (the strongest interaction passes the lower interaction threshold); and 11 (the strongest interaction passes the higher interaction threshold). Hydrogen bonds between polar atoms are calculated using a method based on protein contact statistics, whereby a pair of atoms is scored by distance and orientation. Surface contact interactions are determined by calculating the solvent-exposed surface area of the residue, first in the absence and then in the presence of the ligand. The difference between the two values is the extent to which the ligand has shielded the residue from exposure to solvent, which is potentially indicative of a hydrophobic interaction. The solvent-exposed surface area is determined by adding 1.4 Å to the van der Waals radii of each heavy atom, and computing the fraction of this total surface that does not lie within the radius of any other. The default MOE values were set for preparing and generating PLIF: receptor atoms; MinScore1 = 1 and MinScore2 = 10 for all interactions except ionic interactions (MinScore1 = 5) and surface contacts (MinScore1 = 20 and MinScore2 = 50); maximum number of bits = 250. No activity values were employed in PLIF because of the limited number of compounds used.

Flexible alignment: This is a stochastic search procedure that simultaneously searches the conformational space of a collection of molecules and the space of alignments of those molecules. It flexibly aligns small molecules by maximizing steric and feature overlap. Each alignment is given a score that quantifies the quality of the alignment in terms of both internal strain and overlap of molecular features. The similarity terms used in flexible alignment were: hydrogen bond acceptor, aromatic atoms, and volume

(shape of the molecules). Default settings were used for the remaining parameters. In the first step of the flexible alignment procedure, the strongest dually active compounds (**I49**, **P47**, and **Q40**; Tables 1, 3, and 4) of the subsets were analyzed. The selected alignment of these three compounds has the lowest strain energy and the third-best overall score of the resulting alignments. These three representatives of the subsets were then used as templates for further flexible alignment of all compounds. In the second step, all compounds of the subsets were aligned on the fixed rigid structure of the corresponding dual active representative. This step was performed with the svl script "align all", in which all compounds in the database were aligned pairwise on the rigid structure of the first molecule. As only one result is reported for each aligned molecule, the alignment was repeated in cases where the common substructure of the class was not aligned in the same way. The partial charges of the final aligned structures were then calculated by MOPAC2007 (single point, no optimization, "RM1" and "MMOK" keywords).

CoMFA and CoMSIA settings: The standard settings were used in the CoMFA calculations: 2 Å regular grid size in all three directions within the automatically created grid box, with 4 Å extension beyond the van der Waals volume of the overlaid molecules, sp³ carbon probe with +1 charge, a distance dependent (1/*r*) dielectric constant. The following fields were calculated in CoMFA: steric (s), electrostatic (e), both (b), and hydrogen bond (h-bnd). The RM1 point charges were used for calculation of the electrostatic fields. The standard energetic cutoff value of 30 kcal mol⁻¹ with no electrostatic interactions at bad steric contacts was used. The threshold column filtering was set to 1.0 kcal mol⁻¹. In CoMSIA the following similarity indices fields were calculated: steric (s), electrostatic (e), hydrophobic (h), hydrogen bond donor (d), hydrogen bond acceptor (a), and donor-acceptor (da) with the default attenuation factor of 0.3 in the same grid box as used for CoMFA. A common probe atom with 1 Å radius and charge, hydrophobicity, and hydrogen bond properties of +1 was used. The indices were evaluated according to the usual CoMSIA protocol with 1.0 kcal mol⁻¹ column filtering. The predictive power of the models was evaluated first by LOO cross-validation based on the cross-validated coefficient (*q*²), the optimal number of components (*n*_{opt}), and the predictive sum of squares (PRESS). In the second step, the models were further analyzed by LMO cross-validation, first subdividing the compounds into five groups and then into three groups. Due to the random selection of the compounds in the cross-validation runs, the results can vary. To get more representative values, each run was repeated 20 times, and the results were reported as mean value (*q*²_{mean}) and standard deviation (SD). Visualization of the best achieved model for the selectivity is presented as SD*coefficient contour plots (80% favored, 20% disfavored level) and illustrates regions where variability in molecular fields explains differences in target properties.

Acknowledgements

I.K.P. and M.W. gratefully acknowledge the Alexander von Humboldt Foundation for generous financial support of this study. I.K.P. also thanks the Bulgarian NSF.

Keywords: ABC transporters · molecular modeling · protein–ligand interactions · structure–activity relationships

- [1] H. Glavinas, P. Krajcsi, J. Cserepes, B. Sarkadi, *Curr. Drug Delivery* **2004**, *1*, 27–42.
- [2] G. A. Altenberg, *Curr. Med. Chem. Anticancer Agents* **2004**, *4*, 53–62.
- [3] A. Boumendjel, H. Baubichon-Cortay, D. Trompier, T. Perrotton, A. Di Pietro, *Med. Res. Rev.* **2005**, *25*, 453–472.
- [4] M. Wiese, I. K. Pajeva, *Curr. Med. Chem.* **2001**, *8*, 685–713.
- [5] G. Ecker, P. Chiba, in: *Computational Toxicology: Risk Assessment for Pharmaceutical and Environmental Chemicals* (Ed.: S. Ekins), John Wiley & Sons, Hoboken, **2007**, pp. 295–314.
- [6] I. K. Pajeva, M. Wiese, *AAPS J.* **2009**, DOI: 10.1208/s12248-009-9118-z.
- [7] S. Wang, H. Ryder, I. Pretswell, P. Depledge, J. Milton, T. C. Hancox, I. Dale, W. Dangerfield, P. Charlton, R. Faint, R. Dodd, S. Hassan, *Bioorg. Med. Chem. Lett.* **2002**, *12*, 571–574.
- [8] S. Wang, N. C. Wan, J. Harrison, W. Miller, I. Chuckowree, S. Sohal, T. C. Hancox, S. Baker, A. Folkes, F. Wilson, D. Thompson, S. Cocks, H. Farmer, A. Boyce, C. Freathy, J. Broadbridge, J. Scott, P. Depledge, R. Faint, P. Mistry, P. Charlton, *J. Med. Chem.* **2004**, *47*, 1339–1350.
- [9] S. Wang, A. Folkes, I. Chuckowree, X. Cockcroft, S. Sohal, W. Miller, J. Milton, S. P. Wren, N. Vicker, P. Depledge, J. Scott, L. Smith, H. Jones, P. Mistry, R. Faint, D. Thompson, S. Cocks, *J. Med. Chem.* **2004**, *47*, 1329–1338.
- [10] S. G. Aller, J. Yu, A. Ward, Y. Weng, S. Chittaboina, R. Zhuo, P. M. Harrell, Y. T. Trinh, Q. Zhang, I. L. Urbatsch, G. Chang, *Science* **2009**, *323*, 1718–1722.
- [11] B. H. Norman, P. A. Lander, J. M. Gruber, J. S. Kroin, J. D. Cohen, L. N. Jungheim, J. J. Starling, K. L. Law, T. D. Self, L. B. Tabas, D. C. Williams, D. C. Paul, A. H. Dantzig, *Bioorg. Med. Chem. Lett.* **2005**, *15*, 5526–5530.
- [12] C. Globisch, I. K. Pajeva, M. Wiese, *ChemMedChem* **2008**, *3*, 280–295.
- [13] S. Ekins, R. B. Kim, B. F. Leake, A. H. Dantzig, E. G. Schuetz, L. B. Lan, K. Yasuda, R. L. Shepard, M. A. Winter, J. D. Schuetz, J. H. Wikel, S. S. Wrighton, *Mol. Pharmacol.* **2002**, *61*, 964–973.
- [14] I. K. Pajeva, M. Wiese, *J. Med. Chem.* **2002**, *45*, 5671–5686.
- [15] I. K. Pajeva, C. Globisch, M. Wiese, *J. Med. Chem.* **2004**, *47*, 2523–2533.
- [16] C. Globisch, I. K. Pajeva, M. Wiese, *Bioorg. Med. Chem.* **2006**, *14*, 1588–1598.
- [17] C. Chang, S. Ekins, P. Bahadduri, P. W. Swaan, *Adv. Drug Delivery Rev.* **2006**, *58*, 1431–1450.
- [18] N. R. Tawari, S. Bag, M. S. Degani, *J. Mol. Model.* **2008**, *14*, 911–921.
- [19] T. W. Loo, D. M. Clarke, *J. Biol. Chem.* **2002**, *277*, 44332–44338.
- [20] T. W. Loo, M. C. Bartlett, D. M. Clarke, *J. Biol. Chem.* **2003**, *278*, 50136–50141.
- [21] V. Lather, A. K. Madan, *Bioorg. Med. Chem. Lett.* **2005**, *15*, 4967–4972.
- [22] W. Klinkhammer, H. Müller, C. Globisch, I. K. Pajeva, M. Wiese, *Bioorg. Med. Chem.* **2009**, *17*, 2524–2535.
- [23] P. Borst, R. Evers, M. Kool, J. Wijnholds, *Biochim. Biophys. Acta Biomembr.* **1999**, *1461*, 347–357.
- [24] F. J. Sharom, *Pharmacogenomics* **2008**, *9*, 105–127.

Received: July 14, 2009

Revised: August 19, 2009

Published online on September 18, 2009